JOURNAL OF MATERIALS SCIENCE 21 (1986) 1828–1836

The elastic properties of ion-implanted silicon

P. J. BURNETT, G. A. D. BRIGGS
Department of Metallurgy and the Science of Materials, University of Oxford, Parks Road, Oxford OX1 3PH, UK

The elastic properties of silicon implanted with As^+ and Si^+ in the dose range 10^{14} to 10^{15} ion cm^{-2} has been investigated. Reflection scanning acoustic microscopy techniques have been used to determine changes in the velocity of surface elastic waves (Rayleigh waves) on ion-implanted silicon. With the aid of theoretical models for this mode of wave propagation, the experimental velocity changes have been interpreted in terms of changes in the elastic constants of the implanted layer. These changes have been found to be dependent upon the level of radiation damage produced by the implantation process. Decreases of $\sim 30\%$ in the bulk and shear elastic constants have been deduced for damage levels present at the onset of implantation-induced amorphization.

1. Introduction

Ion implantation is a surface-treatment process that is finding an increasing number of applications for an increasingly wide range of materials. Ion implantation is being extensively used in the doping of semiconductor devices (e.g. see [1]) and, more recently, is finding increasing applications as a process to modify the mechanical and oxidation/corrosion properties of metals (e.g. [2]) and ceramics (e.g. [3]). In both ceramics and semiconductors (which, being brittle, are often regarded as ceramics) the surface stress generation that generally accompanies implantation can have been profound effects upon the mechanical and electrical properties of these materials. Surface stresses principally result from volume increases due to the production of defects (see [4, 5]). Although several attempts at modelling the stresses have been made (e.g. [4, 5]) these have primarily concentrated upon defect formation and neglected the possibly large effects that implantation-induced changes in elasticity might produce.

This paper attempts to clarify the effects of ion implantation upon the elastic constants of silicon implanted with As^+ and Si^+ in the dose range 10^{14} to 10^{15} ion cm^{-2}. These doses resulted in a range of structural changes (including amorphization) within the surface which were characterized theoretically and monitored experimentally (using microhardness testing). Surface elastic wave (Rayleigh wave) velocity measurements have been made using acoustic microscopy techniques and these data correlated with structural changes in the near-surface region. With the aid of theoretical models the elasticity changes in the surface layer have been derived. Finally, the possible consequences of these changes in elasticity upon the stress–dose dependence in semiconductors has been discussed.

2. Background theory

2.1. Ion implantation

Ion implantation is a low vacuum ($< 10^{-5}$ torr) surface-treatment process whereby ions, which have been accelerated through typically 50 to 500 keV, impinge upon and bury themselves in the surface of a target. The ions travel typically $< 0.5\,\mu m$ into the target before coming to rest, losing their kinetic energy in two ways. Firstly, and most importantly, displacement collisions occur, atoms of the target material being displaced either by the incident ions themselves ("primary displacements") or by target atoms that have themselves been displaced ("secondary displacements") (see [6]). Secondly, a relatively small amount of energy is given up by electronic excitation (ionization, etc., see [6]). The implanted ions eventually come to rest in an approximately Gaussian fashion beneath the surface, often the profile being slightly skewed towards the surface when the masses of the incident ions and target atoms are very dissimilar [7]. The damage distribution beneath the surface is of a similar form to that of the concentration profile, being approximately Gaussian. However, in this case, the peak of the damage profile lies rather closer to the surface than that of the concentration profile (see Fig. 1). Both of these profiles are calculable using currently available computer codes. In this study, the EDEP-1 code [8] has been used to evaluate the projected range and damage parameters (R_p, $\langle X_d \rangle$, the concentration and damage profile peaks and ΔR_p, $\langle \Delta X_d \rangle$, the range and damage straggling; see Fig. 1).

For certain materials, notably semiconductors and ceramics, the accumulation of displacement damage as implantation proceeds can result in the target being rendered amorphous once some critical damage threshold is exceeded [3, 9–12]. Clearly, this amorphous material will initially be formed where the level of displacement damage is greatest [10, 11], i.e. at the peak of the damage profile, resulting in the formation of a sub-surface amorphous layer. As the damage level is increased this region will thicken as more of the damage profile exceeds the critical displacement level for amorphization. Eventually, a surface amorphous layer will result. Christel *et al.* [9] have determined

0022-2461/86 $03.00 + .12 © *1986 Chapman and Hall Ltd.*

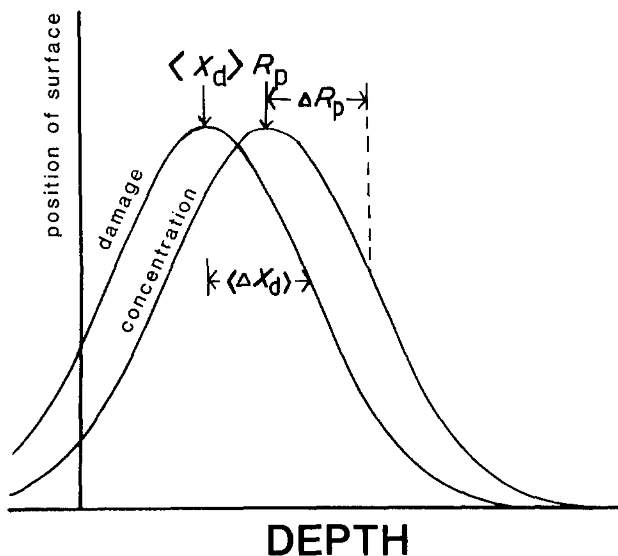

Figure 1 A schematic representation of the shape and relative positions of the concentration and radiation damage profiles produced by ion implantation. The range and damage parameters are also marked, where R_p is the peak concentration, $\langle X_d \rangle$ the peak damage level and ΔR_p, $\langle \Delta X_d \rangle$ their respective standard deviations.

that, for room-temperature implantation into silicon, approximately 15% of the target atoms must be displaced (corresponding to energy deposition levels of 10^{20} to $10^{21}\,\mathrm{keV\,cm^{-3}}$ [9]) in order for amorphous material to be formed. Assuming a Gaussian damage profile and knowing the critical damage level, it is possible to determine the thickness of the amorphous layer, t_a, as follows [13];

$$t_a = \langle \Delta X_d \rangle [8(\ln \phi - \ln \phi_{crit})]^{1/2} \quad (1)$$

for $t_a/2 < \langle X_d \rangle$, $\phi > \phi_{crit}$, (i.e. sub-surface)

$$t_a = \langle X_d \rangle + 0.5 \langle \Delta X_d \rangle [8(\ln \phi - \ln \phi_{crit})]^{1/2} (2)$$

for $t_a/2 > \langle X_d \rangle$, $\phi > \phi_{crit}$, (i.e. surface layer)

where ϕ is the ion dose and ϕ_{crit} is that dose at which amorphization first occurs and may be determined either empirically (as in previous studies e.g. [9–12]) or determined form critical displacement damage data (available in the literature, e.g. [9, 12]) using the following relationship [11];

$$\phi_{crit} = \varrho_{Ecrit} \langle \Delta X_d \rangle (2\pi)^{1/2}\, 10^{-4}/E_c \quad (3)$$

where ϱ_{Ecrit} is the critical damage level ($\mathrm{keV\,cm^{-3}}$), $\langle \Delta X_d \rangle$ is the damage straggling (μm), and E_c is the displacement damage per ion (keV) (this quantity is also calculated by EDEP-1).

Equations 1 to 3 have been used to determine the extent of amorphous material present in the specimens used in this study (see Section 3).

At the doses beneath those at which amorphization occurs, defect structures such as voids, dislocation loops, etc., are commonly found [14, 15], together with the point defects (e.g. Frenkel pairs) initially formed by the incoming ions. The density of these defects is dependent upon dose, usually being a maximum immediately before amorphization. Associated with the formation of these defects and/or amorphous layers are marked changes in the mechanical properties of the implanted layer. Radiation hardening has been observed at pre-amorphization doses, whilst amorphization generally results in a softening of the surface (e.g. [10–13]). Considerable compressive stresses often occur within the layer [4, 5, 16, 17], these arising from the implanted layer attempting to expand in order to accommodate both the defects generated and the incident ions. These stresses can markedly alter the indentation fracture behaviour of brittle materials [5, 10–13].

Given the above description of the radiation damage processes and ensuing mechanical properties changes it is expected that, in addition to plasticity/fracture changes associated with the defective/amorphous layer, there should also be marked changes in elasticity. Since ion implantation into silicon results in the rupturing of bonds, as atoms are displaced from their structure sites, then, assuming that total reconstruction of the disrupted bonds does not occur, the elastic constants of the surface would be expected to decrease in some manner with increasing radiation damage. Investigation of these changes is possible using acoustic microscopy. This will now be described.

2.2. Reflection acoustic microscopy

Reflection acoustic microscopy techniques (see [18, 19] for details of the instruments and mode of operation) have been used in this study to determine the changes in the elastic properties of the implanted surfaces via surface elastic wave (Rayleigh wave*) velocity changes. In scanning acoustic microscopy (SAM) little contrast is observed between regions of differing elastic properties at focus. However, strong contrast arises when the specimen is moved towards the lens (termed "negative defocus") [18, 19], and is dependent upon the particular variation of detected signal (V) with negative defocus (z) for a given material. This function is known as $V(z)$ and has been shown to be dependent upon the Rayleigh wave velocity, v_r. Fig. 2a shows the typical form of this $V(z)$ function. For a material capable of supporting surface elastic waves, the $V(z)$ function shows regular oscillations that occur as a result of interference between the normally reflected ray and reradiating surface waves [20]. The velocity of these surface waves (termed "leaky" Rayleigh waves) will determine the periodicity of the $V(z)$ [20]. The relationship between the $V(z)$ periodically, Δz, and the Rayleigh velocity has been determined [20] as

$$\Delta z = \lambda_w / [2(1 - \cos \theta_R)] \quad (4)$$

where λ_w is the wavelength in water, θ_R the critical angle for Rayleigh wave excitation which $= \sin^{-1}$ (wave velocity in water/Rayleigh velocity). The detailed form of the $V(z)$ curves are determined not only by the Rayleigh velocity (which determines

*These waves are a mixture of longitudinal and shear wave motion, are bound to the surface and decay exponentially with depth. In the presence of a fluid (as here), Rayleigh waves can couple to bulk waves in the fluid.

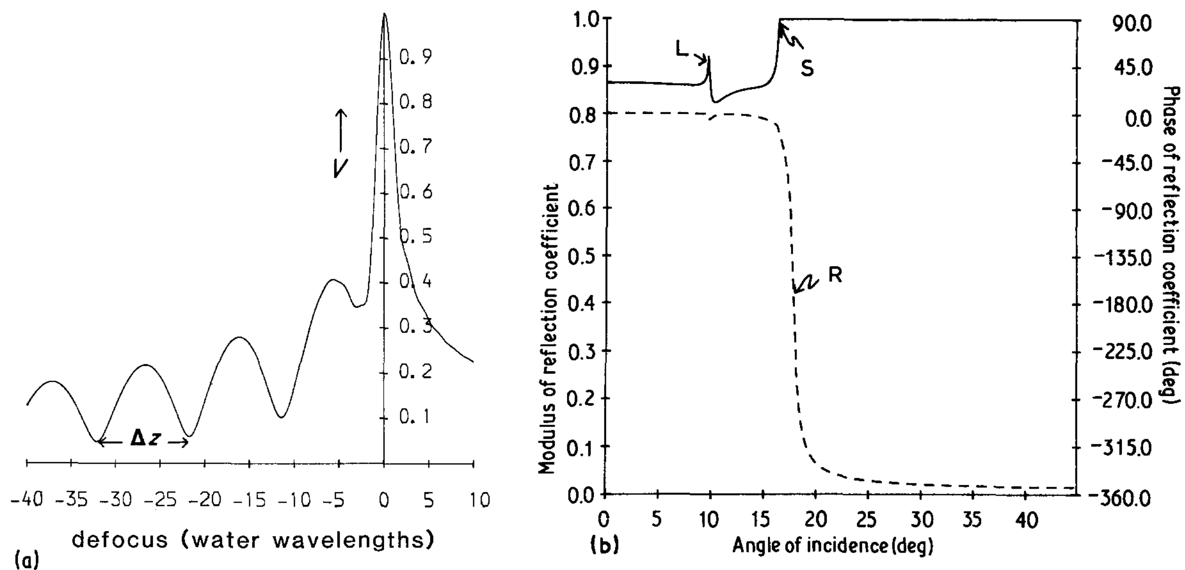

Figure 2 (a) The theoretical $V(z)$ for silicon calculated from the reflectance function in (b). Note the regular periodicity (Δz) which is determined by the Rayleigh velocity (see text). (b) The complex reflectance function calculated for silicon (assumed isotropic) showing both the modulus (solid line) and phase (broken line). Also marked are the critical angles for longitudinal wave excitation (L), shear wave excitation (S) and Rayleigh wave excitation (R). These appear as discontinuities in the phase and modulus of the reflectance function.

periodicity) but by the geometry of the acoustic and the angular lens response (termed the "pupil function", $P(\theta)$). The expression given by Sheppard and Wilson [21] for $V(z)$ is;

$$V(z) = 1/2\pi \int_0^\alpha P(\theta) R(\theta) \times \exp(2ikz \cos\theta) \cos\theta \sin\theta \, d\theta \quad (5)$$

where θ is the angle of incidence, α the semiangle of the lens aperture, k the incident wave vector, z the defocus, $\sin\theta \cos\theta$ is a term accounting for the (spherical) lens geometry, $P(\theta)$ is the pupil function defined to account for two way passage through the lens, and $R(\theta)$ is the reflectance function of the specimen surface. The reflectance function, $R(\theta)$, is complex, containing both phase and amplitude information and can be calculated by solving the acoustic Fresnel equations (see [22]). Fig. 2b shows the calculated reflectance function used to evaluate the $V(z)$ shown in Fig. 2a.

$V(z)$ will differ for materials of differing Rayleigh velocity, thus at negative defocus, contrast will arise between elastically dissimilar materials as a result of the $V(z)$s becoming out of phase with each other (Fig. 3). In addition, this contrast is observed to reverse as the defocus is changed (see Fig. 3). Hence, $V(z)$ measurements can provide a sensitive means of characterizing bulk materials properties (e.g. [23]).

Other workers have used measurement of $V(z)$ periodicities to characterize layered structures (e.g. [23, 24]. For the case where layer thickness is much less than the Rayleigh wavelength† ($h \ll \lambda_R$) the form of the $V(z)$ remains similar to that of the unimplanted surface, with only small (< 5%) shifts in the periodicity occurring [24]. However, when $h \gtrsim \lambda_R$ then the $V(z)$ can be markedly different. In certain cases additional surface wave/waveguide modes may be excited [25] and the $V(z)$ then contains several periodicities. Simple periodicity measurement is impossible in these situations and Fourier analysis of the $V(z)$ has to be used to determine spatial frequencies present (e.g. [23]).

In bulk specimens Rayleigh waves are non-dispersive (i.e. v_R is independent of frequency). However, for layered specimens this is not so, the influence of a given surface layer upon v_R (and hence $V(z)$) will be frequency dependent. The dispersion relationship for v_R of given layered structures can be computed [22, 25] and provides a means of film thickness determination from measured velocity changes at specific frequencies (e.g. see [24]). Dispersion relationships (via $V(z)$ measurements) for several systems, together with film thickness determinations, have been reported in the literature (e.g. [26, 27]).

The dispersive nature of layered media can be exploited in this study. Since, for our ion-implanted specimens, both the frequency and layer thickness are known, the elastic properties of ion-implanted silicon surfaces can be determined from measurements of Rayleigh velocity. At the frequencies used in this study (550 MHz) the ion-implanted layer approximates to the case where $h \ll \lambda_R$, where h is typically $< 0.3\,\mu$m and λ_R is typically $10\,\mu$m. As described in Section 2.1, the accumulation of radiation damage is expected to exert greatest influence over the elastic properties of the surface, and further, that this damage has a Gaussian profile. This profile will be approximated to as three discrete layers, the depth of whose interfaces are defined by the surface, half-maximum-height of the Gaussian and finally twice $\langle X_d \rangle + 2\langle \Delta X_d \rangle$ as shown schematically in Fig. 4. Where amorphous layers are present the 1/2-max-height boundaries will be replaced by the calculated depths of the amorphous/crystalline interfaces.

†Because of the exponential decay, a Rayleigh wave may be considered to sample the elastic properties of a layer approximately one wavelength thick.

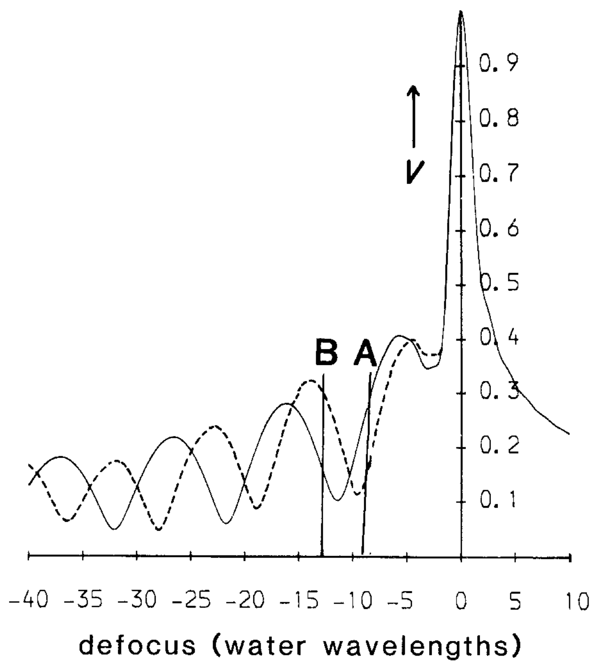

Figure 3 Illustration of the manner in which contrast in the scanning acoustic microscope varies with defocus for two elastically dissimilar materials. The two $V(z)$s shown are for silicon (solid line) and silicon with an aluminium layer 0.05 wavelengths thick. The two $V(z)$s have different periodicities which results in them becoming progressively out of phase as the defocus is increased. Marked on this figure are two points at which the contrast is strong; however, the contrast at A will be the reverse of that at B.

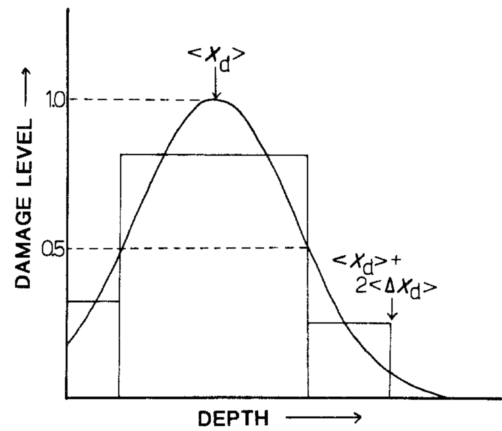

Figure 4 For ease of calculation, the Gaussian damage profile has been modelled as three discrete layers the depth of whose boundaries are determined by the surface, the positions of half-maximum-height and $\langle X_d \rangle + 2\langle \Delta X_d \rangle$. The damage level for each layer is the mean damage level for that section of Gaussian (i.e. the areas are equal).

3. Experimental techniques

3.1. Ion implantation

Six wafers of near (0 0 1) surface ($\pm \sim 3°$) silicon were ion implanted (courtesy of British Telecom Research Laboratories, Martlesham Heath, UK) with 180 keV Si^+ or As^+ to doses in the range 10^{14} to 10^{15} ion cm^{-2}. Table I gives the projected range and damage profile parameters evaluated using the Harwell version of EDEP-1 together with the doses for each wafer. The doses were chosen to yield a range of damaged/ amorphous structures ranging from mildly damaged (10^{14} Si^+ cm^{-2}) through specimens expected to possess a sub-surface amorphous layer (e.g. 2×10^{14} As^+ cm^{-2}), to a specimen with a surface amorphous layer (10^{15} As^+ cm^{-2}). These specimens were supplied as 3 in. (75 mm) wafers of which one-half was masked during the implantation. Using Tolanski interferometry (green light) no surface steps were observed across the implanted/unimplanted boundary (i.e. any surface step present must be less than ~ 25 nm). This is in agreement with other workers [28] who also failed to detect any surface lifting in this dose range. The predicted amorphous layer thicknesses (if present) were evaluated using the approach of Section 2.1 and are also detailed in Table I.

3.2. Acoustic microscopy

Both imaging scanning acoustic microscopy and $V(z)$ aquisition were performed on the Oxford SAM operating at 550 MHz with a sapphire lens of focal length 280 μm and aperture semi-angle of 36°. Water at room temperature was used to couple this lens to the specimen surface in all cases. Electronic image processing was usually used to enhance image contrast. The periodicities present in the experimentally determined $V(z)$s (an example of which is shown in Fig. 5) were determined in the following manner (see also Fig. 5).

1. The first three clearly defined ripples beyond focus were selected.

2. The distance between the 1st and 3rd minima was measured.

3. The distance determined in (2) was calibrated against the water ripple§. Since this is a function only

TABLE I Implantation parameters

Specimen	Dose (ion cm^{-2})	Range parameters		Damage paramters		Microstructural state (amorphous?)
		R_p (μm)	ΔR_p (μm)	$\langle X_d \rangle$ (μm)	$\langle \Delta X_d \rangle$ (μm)	
As-1	10^{14} As^+					crystalline
As-2	2×10^{14} As^+	0.1	0.035	0.059	0.039	sub-surface (0.085 μm)
As-3	10^{15} As^+	(damage per ion = 92 keV)				surface (0.14 μm)
Si-1	10^{14} Si^+					crystalline
Si-2	2×10^{14} Si^+	0.244	0.074	0.159	0.103	crystalline
Si-3	10^{15} Si^+	(damage per ion = 60 keV)				sub-surface (0.27 μm)

§"Water ripple" is a short periodicity, regular oscillation superimposed upon the $V(z)$ visible in Fig. 5. It results from interference between internal lens reflections and the normally reflected component of the signal and has a periodicity of $\lambda_w/2$.

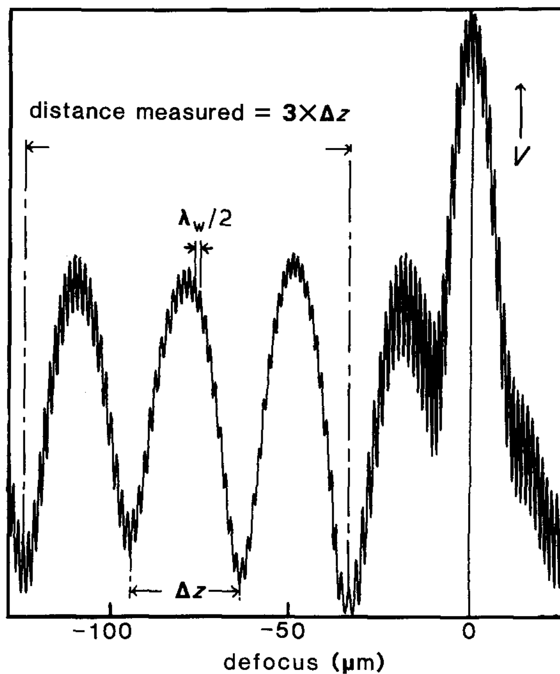

Figure 5 An experimentally determined (unfiltered, 550 MHz) $V(z)$ for silicon implanted with 10^{15} Si^{+} cm^{-2} showing (i) the three long-period ripples from which the Rayleigh velocity was determined, and (ii) the fine "water ripple" (of periodicity $\lambda_w/2$) superimposed upon the $V(z)$.

of the properties of water and the lens geometry, errors in periodicity due to mechanical/electrical instabilities in the motor-driven stage will be eliminated.

4. The measured periodicity (now in water ripples) was converted to Rayleigh velocity using Equation 4 and, to allow easy comparison with the theoretical calculations, normalized against the calculated Rayleigh velocity of the virgin silicon (see Section 4 for parameters used in this calculation).

The above procedure was used on raw data only, but for general comparisons the $V(z)$s in this paper have been low-pass filtered (e.g. Fig. 7) (using a moving average procedure) to remove the water ripple.

In addition to aquisition of $V(z)$ curves of the type shown in Figs. 2 and 5, the $V(z)$ was also recorded "pictorially" by simultaneously fast scanning the lens in the x-direction whilst defocusing in the z-direction. For a uniform material, these $V(z, x)$s consist of horizontal bright and dark bands corresponding to the peaks and troughs of the $V(z)$s. However, when $V(z, x)$s are taken across the boundary of two dissimilar materials, at the boundary the fringes will no-longer match. The degree of this mis-match allows a quick, qualitative, visual determination of the levels of contrast to be seen in an image.

3.3. Hardness testing

A Matsuzawa microhardness tester was used to determine the microhardness of all the specimens studied. A Knoop profile indenter, with its long diagonal aligned along a ⟨1 0 0⟩ surface direction was used for all tests. Loads of 10 gf and 25 gf were utilized in order to produce indentations (10 to 20 μm long diagonal)

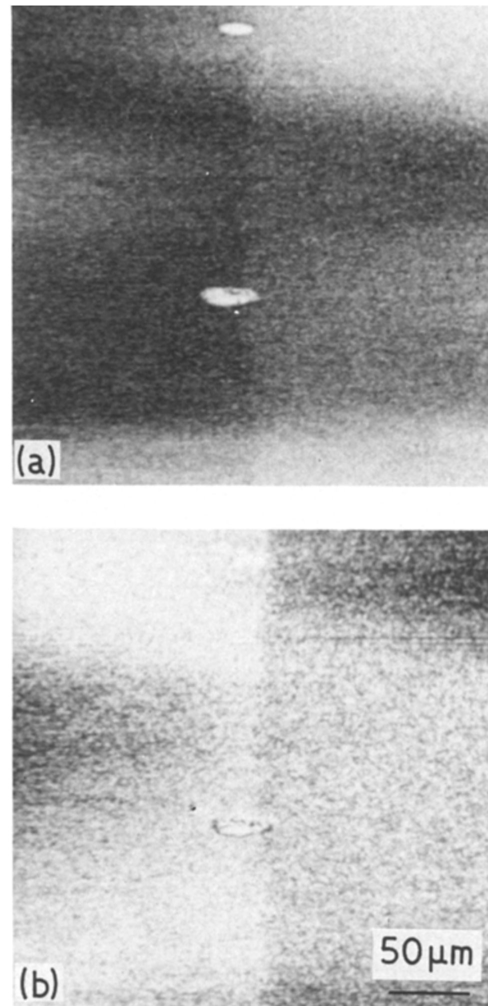

Figure 6 Acoustic images of the implanted/unimplanted boundaries of silicon implanted with 10^{15} As^{+} cm^{-2} at 180 keV. The feature in the centre of the micrograph is a Knoop microhardness indentation placed for reference. (a) -30 μm, (b) -40 μm defocus at 550 MHz.

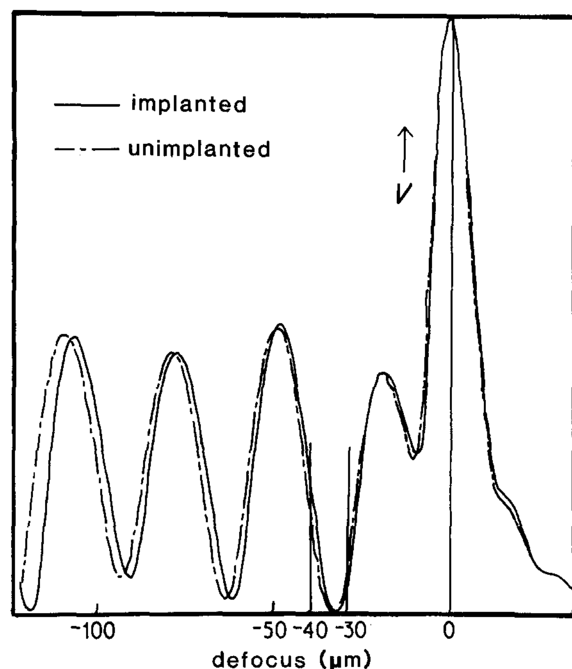

Figure 7 Experimentally determined (low-pass filtered, 550 MHz) $V(z)$s for unimplanted and 10^{15} As^{+} cm^{-2} implanted silicon. Marked are the defoci used to obtain the images shown in Fig. 6.

which lay substantially within the implanted layers (see [10, 11] for details of this approach).

4. Results and discussion

As described in Section 2, it is expected that ion implantation will result in the formation of a less stiff surface layer. The effect of this upon surface wave propogation will be to lower the Rayleigh velocity, v_R, on that surface [25]. These changes in v_R are expected to produce contrast in the acoustic microscope at some negative defocus (see Section 2.2). Consequently, for each specimen, a series of images (at 550 MHz) were taken over areas containing both implanted and unimplanted material. Fig. 6 shows typical images (for $10^{15}\,As^+\,cm^{-2}$ implantation), Fig. 6a being taken at $-30\,\mu m$ defocus and Fig. 6b at $-40\,\mu m$ defocus. It can be seen that the contrast reverses as the defocus is changed. Fig. 7 shows the $V(z)$ curves recorded for the implanted and unimplanted regions shown in Fig. 6, the defoci at which Figs. 6a and b were recorded also being marked. The $V(z)$ of the implanted material is slightly out of step with that of the unimplanted material, and it is this that gives rise to the (albeit) weak contrast observed between the two regions. Images of this type were recorded for all but the lowest dose silicon-implanted specimen ($10^{14}\,Si^+\,cm^{-2}$). Here no contrast was observed.

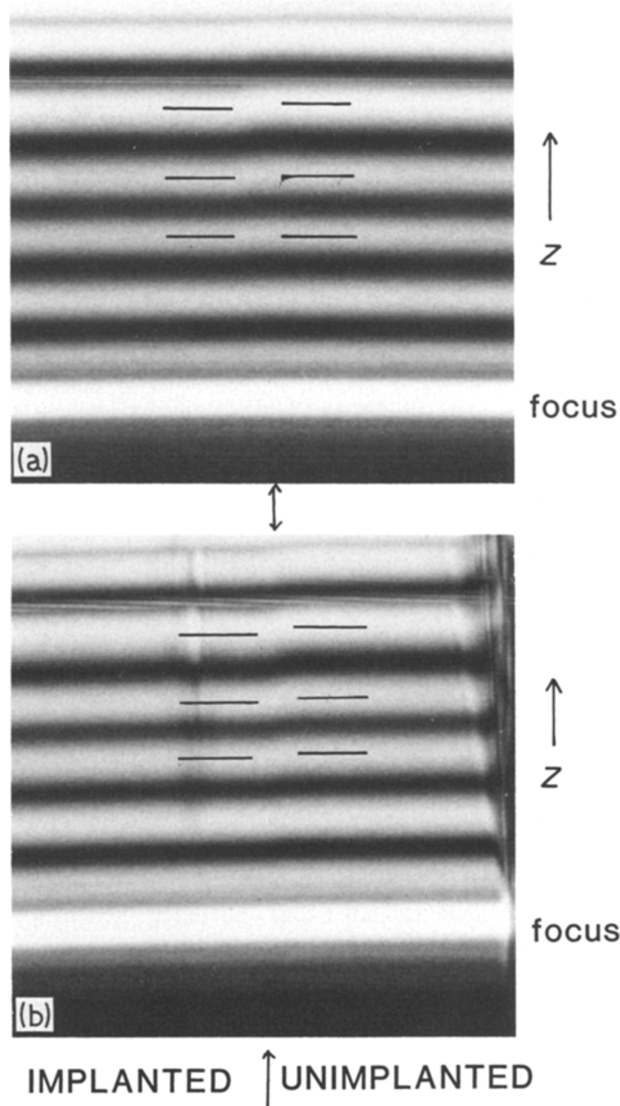

Figure 8 $V(z, x)$s recorded across implanted/unimplanted boundaries such as those shown in Fig. 6 for silicon implanted to (a) $2 \times 10^{14}\,Si^+\,cm^{-2}$, (b) $10^{15}\,As^+\,cm^{-2}$. Note that a greater degree of fringe shift can be seen in (b) than in (a), indicating a greater "loading" of the substrate by the implanted layer. The large feature to the right of (b) is a surface scratch.

TABLE II Experimental and calculated Rayleigh velocities

Specimen	Rayleigh velocity ($m\,sec^{-1}$)	
	Experimental	Calculated
Unimplanted	4888 ± 5	4888
As-1	4865	4868
As-2	4852	4860
As-10	4845	4855
Si-1	4878	4877
Si-2	4871	4866
Si-10	4825	4819

Figs. 8a and b show the $V(z, x)$s recorded across the implanted/unimplanted boundaries (such as those imaged in Fig. 6) for silicon implanted with Si^+ at 2×10^{14} and $10^{15}\,ion\,cm^{-2}$, respectively. Some fringe offset can be seen across the boundary in Fig. 8b (high dose) and a less readily detectable shift can be seen in Fig. 8a, i.e. this specimen would not be expected to show as much contrast across the implanted/unimplanted boundary when imaged, as was the case.

From the recorded $V(z)$s the Rayleigh velocities were determined using the method described in Section 3.2 and the derived values are presented in Table II. It can be seen that the general trend in these figures can be correlated with the calculated levels of radiation damage and the presence and size of an amorphous layer, i.e. the greater the damage the slower the surface. The accuracy of these velocities depends upon several factors. Most important of these is the assumption that the water ripple periodicity remains constant. Temperature variations will affect the velocity of sound in water and would thus affect the water ripple periodicity. Although no temperature control was used in these experiments, the changes in velocity that would result from normal room temperature variations ($< 5°\,C$) would only change the water velocity by $\sim 0.6\%$ [29]. Periodicity measurement uncertainties are expected to be a greater source of error. It is estimated that the $V(z)$ periodicity measured over three periods) can be measured to $\sim 1\%$. Indeed, the periodicities measured for unimplanted silicon on six independent $V(z)$s (one acquired from the unimplanted region of each of the six specimens studied here) yielded an average periodicity of 62.9/3 water ripples with standard deviation of only 0.11/3 water ripples. This deviation has been used to estimate the error in v_R as approximately $\pm 5\,m\,sec^{-1}$ (± 1 S.D.).

Before discussing these results further, it was considered judicious to confirm that the calculations/predictions concerning amorphous layer thickness were not substantially in error by using low-load hardness testing. These tests can qualitatively indicate the extent of amorphous layer present and the data

TABLE III Knoop hardness results

Specimen	Knoop hardness* (KNH)		Comments
	10 gf load	25 gf load	
Unimplanted	763 (725-804)	857 (822-894)	
As-1	884 (752-1053)	921 (895-950)	harder
As-2	648 (615-682)	833 (792-879)	intermediate
As-10	736 (699-777)	750 (706-799)	softer
Si-1	872 (881-953)	883 (851-917)	harder
Si-2	836 (793-882)	848 (823-875)	harder?
Si-10	739 (704-778)	842 (822-863)	softer

*Figures in brackets are ± 1 S.D.

obtained in the tests performed here will be interpreted in the light of the structure/hardness relationships previously determined for ion implantation into other brittle materials (see [5, 10, 11] for details); i.e. the surface becomes radiation hardened when no amorphization occurs; amorphous material is softer than the parent material and thus lower hardness is found when a surface layer is present; sub-surface amorphous layers show intermediate hardness values, these lying between the peak radiation-hardened value and the lower values obtained for surface amorphous layers¶. The results of the hardness test performed on the specimens used in this study are shown in Table III and qualitatively support the presence and sizes of amorphous layer predicted, although these data indicate that some amorphous material might be present in the silicon implanted with $2 \times 10^{14}\,Si^+\,cm^{-2}$.

Thus, the structures that the hardness values imply agree well with the predicted structures for the As^+ implanted silicon but less well for the Si^+ implanted silicon. The reasons for this probably lie in the simplicity of the modelling approach used here when compared to the complexity of the implantation process. The critical energy level for amorphization is not a material constant, but depends upon a large number of factors including implantation temperature, dose rate and ion mass. The calculations performed here have assumed a value of $10^{21}\,keV\,cm^{-3}$ as the amorphization threshold. Whilst this seems to work for the As^+ implantation, a lower value would possibly be more appropriate for the Si^+ implant. Alternatively, these discrepancies could arise from both inaccuracies in the damage per ion calculated by EDEP-1 from the assumption of a Gaussian profile. However, the values derived and used in this study are still useful as a guide to the plastic/elastic/microstructural modifications that may result from implantation and are adequate for the present study.

In order to estimate what the actual elastic properties of the ion-implanted/amorphous material are, it was decided to attempt to calculate the changes in

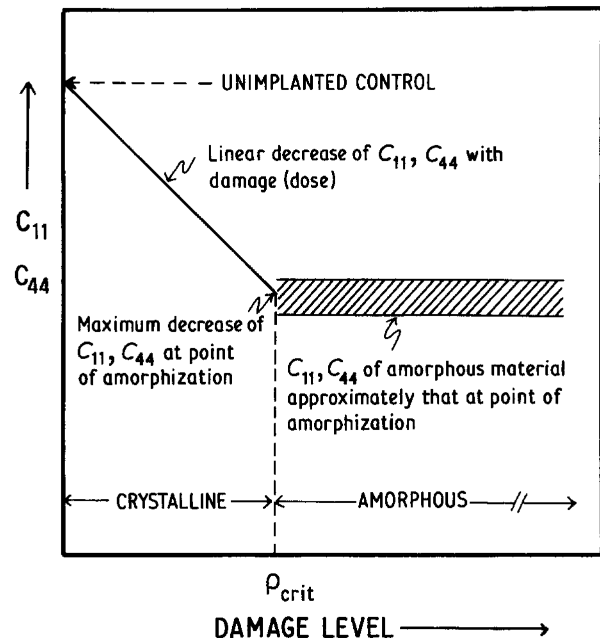

Figure 9 A summary of the variation of C_{11}, C_{44} assumed for the theoretical calculations of v_R on implanted silicon. ϱ_{crit} is the damage level above which the material is rendered amorphous.

Rayleigh velocity that would result from ion implantation. This was achieved by modelling the ion-implanted layer as three discrete layers (see Section 2.2) and using the approach of Brekhovskikh [22] to calculate the reflectance function (and hence Rayleigh angle) for the layered specimen. Here, for simplicity, silicon has been assumed to be both lossless and elastically isotropic. This is not expected to affect the analysis to any great extent since, when using a spherical lens (i.e. sampling Rayleigh waves that are propagating in all directions) a "mean" Rayleigh velocity is determined. In reality, other surface wave modes (including Rayleigh waves of differing, orientation-dependent, velocity) will exist and determine the precise form of the $V(z)$ (e.g. [30]). However, before proceeding further it is necessary to make some crude assumptions concerning the dose dependence of the parameters that govern the Rayleigh velocity in layered media. These are: (i) C_{11} and C_{44} vary linearly with damage level, reaching a minimum at the point of amorphization; (ii) C_{11} and C_{44} of the amorphous material are constant and are close to the values of the crystalline material C_{11} and C_{44} at amorphization; (iii) no density changes occur during implantation. Points (i) and (ii) are summarized in Fig. 9. Assumption (i) seems reasonable since implantation-induced strains in silicon [31, 32] have been reported to vary linearly with dose–this indicates that the defect generation (that we are assuming is responsible for elasticity changes) is a linear function of damage energy (i.e. no *in situ* annealing occurs). Assumption (ii) is difficult to justify, however, in the absence of more detailed information concerning the structure of the amorphous material it is impossible to be any more realistic. Assumption (iii) has been made since (a) no surface step across the implanted/unimplanted boundary was

¶The hardness value measured depends upon the relative volumes of surface-crystalline, sub-surface-amorphous and crystalline-substrate sampled and can vary dramatically depending upon indenter penetration (e.g. see data Si-2 in Table III). No detailed analysis of this is available.

TABLE IV Elastic constants and thickness of layers used in Rayleigh velocity calculations

Specimen	Layer 1		Layer 2		Layer 3	
	C_{11}, C_{44}*	h (μm)	C_{11}, C_{44}*	h (μm)	C_{11}, C_{44}*	h (μm)
As-1	92.5%	0.011	77.0%	0.097	93.4%	0.030
As-2	76.6%	0.017	70%†	0.085	82.3%	0.036
As-10	–	–	70%†	0.140	–	–
Si-1	97.4%	0.024	94.6%	0.270	98.1%	0.071
Si-2	94.9%	0.024	89.2%	0.270	96.2%	0.071
Si-10	74.0%	0.024	70%†	0.270	81.0%	0.071

*The values of elastic constants shown above are expressed as percentages of the values of unimplanted silicon; $C_{11} = 1.865 \times 10^{12}$, $C_{44} = 0.665 \times 10^{12}$ dyn cm^{-2}.
†Amorphous material.

observed, and (b) other workers have also found any volume changes associated with implantation to these dose levels impossible to detect [27]. It is important to realize that since sizeable compressive stresses are generated with implanted layer of this type (e.g. [4, 5, 16]) some accompanying increase in volume must be occurring. However, this expansion is constrained by the underlying and surrounding material in most cases, resulting in minimal changes in density. An estimate of the density change at amorphization may be made from the linear strains observed at amorphization. These have been reported to be $\sim 1\%$ for GaAs, germanium and silicon, this giving a maximum volumetric strain (and hence density decrease) of $\sim 3\%$. This density decrease may be partially compensated for by increases in density due to the injection of additional atoms by the implantation process. However, this is small, being only $\sim 0.8\%$ for the 10^{15} As^+ cm^{-2} implantation. From these figures a surface step of < 2 nm* would be expected, i.e. less than could be detected using two-beam interferometry techniques. Thus, any density changes that do occur are likely to be much smaller than the changes in elasticity.

A range of C_{11}, C_{44} values were used to calculate changes in v_R for the layered structures used to approximate the Gaussian damage profile. Those values that gave reasonable agreement with the experimentally derived values of v_R are given in Table IV together with the layer thickness used whilst the calculated values of v_R are given in Table II. Reasonable agreement with the experimental values of v_R are found when C_{11} and C_{44} of the amorphous layer and substrate-at-point-of-amorphization are taken to be ~ 0.7 those of the parent crystal. The magnitude of this change can be simply interpreted in terms of the number of bonds ruptured by implantation. Christel *et al.* [9] showed that if $\sim 15\%$ of the parent atoms were displaced, amorphization would occur. This corresponds to $\sim 30\%$ of the bonds in the surface being ruptured at amorphization. So, assuming no bond reconstruction, and that the elastic constants of the surface are dependent upon the number of bonds present, a decrease in stiffness of $\sim 30\%$ would also be predicted. Thus, the measured changes in Rayleigh velocity are consistent with a radiation damage-dependent change in elastic properties.

Whilst, perhaps, more accurate calculations could be made using a greater number of layers to model the Gaussian damage profile, and by incorporating anistropy and attenuation terms into the calculations, it is felt that, given the lack of understanding of the damage–elasticity dependence, the additional complexity of such an approach would not be justified here.

Changes in the elastic constants of surfaces during ion implantation can be important in determining the levels of stress generated during implantation. Other workers [31, 32] have shown using X-ray techniques, that the lattice strain varies linearly with dose for implantation into silicon, whereas the stress does not [4]. Stress variation with dose is usually found to vary approximately linearly with dose for doses much less than the amorphization dose. But when the dose approaches the amorphization dose the stress varies sub-linearly. Clearly, variations of elastic constants with dose similar to those described here can account for this behaviour. Similar sub-linear dose dependence of stress has observed for a number of materials (e.g. [34]) and it is possible that changes of elastic constants with dose are making a substantial contribution to this behaviour.

5. Conclusions

The use of acoustic microscopy techniques has enabled estimates of the implantation-induced changes of the elastic properties of silicon to be made. The combination of experimentally determined Rayleigh velocity changes and theoretical modelling has indicated that, at the point of amorphization, the elastic constants, C_{11} and C_{44}, are reduced by approximately 30%. The amorphous material generated by the implantation also shows elastic properties $\gtrsim 30\%$ lower than those of the parent silicon.

Acknowledgements

This work was sponsored by the ALVEY programme. PJB wishes to thank SERC and the ALVEY Directorate for support under this scheme. We wish to thank British Telecom Research Laboratories, Martlesham, for provision of specimens. It is a pleasure to thank Professor Sir Peter Hirsch, FRS for provision of laboratory facilities.

*It is interesting to note that Hubler *et al.* [33], using doses an order of magnitude greater than those here ($> 10^{16}$ ion cm^{-2}) detected surface steps of 10 to 16 nm, i.e. an order of magnitude greater than those expected to result from the implants here.

References

1. G. DEARNALEY, J. H. FREEMAN, R. S. NELSON and J. STEVEN, "Ion Implantation" (North-Holland, Amsterdam, 1973).
2. G. DEARNALEY, *Nucl. Instrum. Meth.* **182/183** (1981) 899.
3. P. J. BURNETT and T. F. PAGE, *Inst. Phys. Conf. Ser.* **75** (1986) in press.
4. E. P. EERNISSE, *J. Appl. Phys.* **45** (1974) 167.
5. P. J. BURNETT and T. F. PAGE, *J. Mater. Sci.,* **20** (1985) 4624.
6. G. CARTER and W. A. GRANT, "Ion Implantation into Semiconductors" (Edward Arnold, London, 1976).
7. K. B. WINTERBON, P. SIGMUND and J. B. SANDERS, *Kgl. Dansk. Vid. Selsk. Mat. Fys. Med.* **37** (14) (1970) 1.
8. I. MANNING and G. P. MUELLER, *Comp. Phys. Commun.* **7** (1974) 85.
9. L. A. CHRISTEL, J. F. GIBBONS and T. W. SIGMON, *J. Appl. Phys.* **52** (1981) 7143.
10. P. J. BURNETT and T. F. PAGE, *J. Mater. Sci.* **19** (1984) 845.
11. *Idem, ibid.* **19** (1984) 3524.
12. J. M. WILLIAMS, C. J. McHARGUE and B. R. APPLETON, *Nucl. Instrum. Meth.* **209/210** (1983) 317.
13. P. J. BURNETT, PhD thesis, University of Cambridge (1984).
14. A. G. CULLIS, T. E. SEIDEL and R. L. MEEK, *J. Appl. Phys.* **49** (1978) 5188.
15. D. J. MAZEY and R. S. NELSON, *Can. J. Phys.* **46** (1968) 687.
16. E. P. EERNISSE, *J. Appl. Phys.* **48** (1977) 3337.
17. N. E. W. HARTLEY, *J. Vac. Sci. Technol.* **12** (1975) 485.
18. G. A. D. BRIGGS, "An Introduction to Scanning Acoustic Microscopy" (Oxford University Press and the Royal Microscopial Society, Oxford, 1985).
19. R. A. LEMONS and C. F. QUATE, in "Physical Acoustics", Vol 14, edited by W. P. Mason and R. N. Thurston (Academic, London, 1979) p. 1.
20. W. PARMON and H. L. BERTONI, *Electron. Lett.* **15** (1979) 684.
21. C. J. R. SHEPPARD and T. WILSON, *Appl. Phys. Lett.* **38** (1981) 858.
22. L. M. BREKHOVSKIKH, "Waves in Layered Media" (Academic, New York, 1980).
23. J. KUSHIBIKI and N. CHUBACHI, *Trans. IEEE* **SU-32** (1985) 189.
24. R. D. WEGLEIN, *ibid.* **SU-32** (1985) 225.
25. G. W. FARNELL and E. L. ADLER, in "Physical Acoustics", Vol 9, edited by W. P. Mason and R. N. Thurston (Academic, London, 1972) pp. 35–127.
26. K. LIANG, S. D. BENNETT, B. T. KHURI-YAKUB and G. S. KING, *Appl. Phys. Lett.* **41** (1982) 1124.
27. R. D. WEGLEIN, *Electron. Lett.* **18** (1982) 1003.
28. E. W. MABY, C. W. MAGEE and J. H. MOREWOOD, *Appl. Phys. Lett.* **39** (1981) 157.
29. R. A. LEMONS, PhD thesis, Stanford University (1975).
30. M. G. SOMEKH, G. A. D. BRIGGS and C. ILETT, *Phil. Mag. A* **49** (1984) 179.
31. V. S. SPERIOSU, H. L. GLASS and T. KOBAYSHI, *Appl. Phys. Lett.* **34** (1979) 539.
32. B. E. MacNEAL and V. S. SPERIOSU, *J. Appl. Phys.* **52** (1981) 3953.
33. G. K. HUBLER, C. N. WADDELL, W. G. SPITZER, J. E. FREDRIKSON and T. A. KENNEDY, **27** (1984) 217.
34. G. B. KREFFT and E. P. EERNISSE, *J. Appl. Phys.* **49** (1978) 2725.

Received 4 October
and accepted 7 November 1985